

# Metal Big Area Additive Manufacturing: Process Modeling and Validation

**Srdjan Simunovic<sup>1</sup>, Andrzej Nycz<sup>1</sup>, Mark W. Noakes<sup>1</sup>, Charlie Chin<sup>2</sup>, and Victor Oancea<sup>2</sup>**

<sup>1</sup>Oak Ridge National Laboratory, Oak Ridge, TN, USA

<sup>2</sup>Dassault Systemés SIMULIA Corporation, Johnston, RI, USA

## 1. Abstract

Metal Big Area Additive Manufacturing (mBAAM) is a new additive manufacturing (AM) technology for printing large-scale 3D objects. mBAAM is based on the gas metal arc welding process and uses a continuous feed of welding wire to manufacture an object. An electric arc forms between the wire and the substrate, which melts the wire and deposits a bead of molten metal along the predetermined path. In general, the welding process parameters and local conditions determine the shape of the deposited bead. The sequence of the bead deposition and the corresponding thermal history of the manufactured object determine the long range effects, such as thermal-induced distortions and residual stresses. Therefore, the resulting performance or final properties of the manufactured object are dependent on its geometry and the deposition path, in addition to depending on the basic welding process parameters. Physical testing is critical for gaining the necessary knowledge for quality prints, but traversing the process parameter space in order to develop an optimized build strategy for each new design is impractical by pure experimental means. Computational modeling and optimization may accelerate development of a build process strategy and saves time and resources. Because computational modeling provides these opportunities, we have developed a physics-based Finite Element Method (FEM) simulation framework and numerical models to support the mBAAM process's development and design. In this paper, we performed a sequentially coupled heat transfer and stress analysis for predicting the final deformation of a small rectangular structure printed using the mild steel welding wire. Using the new simulation technologies, material was progressively added into the FEM simulation as the arc weld traversed the build path. In the sequentially coupled heat transfer and stress analysis, the heat transfer was performed to calculate the temperature evolution, which was used in a stress analysis to evaluate the residual stresses and distortions. In this formulation, we assume that physics is directionally coupled, i.e. the effect of stress of the component on the temperatures is negligible. The experiment instrumentation (measurement types, sensor types, sensor locations, sensor placements, measurement intervals) and the measurements are presented. The temperatures and distortions from the simulations show good correlation with experimental measurements. Ongoing modeling work is also briefly discussed.

## 2. Introduction

The Metal Big Area Additive Manufacturing (mBAAM) extends the capabilities of the additive manufacturing (AM), making it possible to efficiently manufacture large, complex metal objects. The objective is to manufacture large objects that are as close to net shape as practically possible with controllable material properties. Large scale, gas metal arc welding-based AM has been actively pursued in recent years [1-3]. Compared to other metal deposition methods, it has lower capital cost, large build envelope, higher production rates, and a strong established supply chain [2]. This makes it the most economic method to build large parts with medium near net shape accuracy. Increasing shape accuracy has been explored using hybrid deposition and milling methods [4, 5]. Computational modeling is a key technology enabler for wire arc welding-based AM. The Finite Element Method (FEM) simulations have been used extensively in the process development [6]. They involve thermal, mechanical, and metallurgical models that have to deal with evolving geometry, material deposition, and disparate length and time scales. Although not mandatory, the various physics models are usually executed sequentially with the thermal model used as the main driver to assess temperature evolution and metallurgical models for subsequent stress analysis models. Arc welding is a complex multi-physics phenomenon, and its modeling involves many parameters and formulations that are difficult to determine experimentally [7]. Heat source interactions with the feedstock wire and the substrate [8-10], material properties at high temperatures [11, 12], heat transfer mechanisms in the system [13], interactions between the deposited beads [14, 15], etc., have strong effects on the overall result. Therefore, it is necessary to calibrate the computation models on a controlled set of experiments.

In this paper, we present a development of thermo-mechanical computational models for mBAAM and their calibration against experiments. The developed simulations utilize a new physics-based general framework for AM in the general purpose software ABAQUS [16]. The models describe the macroscale heat transfer phenomena in the mBAAM process and the corresponding mechanical response, distortion, and residual stress. The micro-scale details of the surface variation, welding pool dynamics, and material microstructure, etc. are not modeled and are indirectly accounted for by the constitutive material models and heat transfer models.

In the next section, we describe the mBAAM equipment configuration and experiment setup. It is followed by the formulations of the implemented computational models for materials, heat sources, and boundary conditions. The simulation results from the thermal and mechanical models are in the good agreement with the experimental measurements. Ongoing and upcoming work is briefly discussed as it will be extended to the more complex build geometries.

## 3. Experimental Setup

Figure 1 depicts the mBAAM Wolf Robotics station. The station is comprised of a protection work cell, ABB IRB 2600 robotic arm with IRC5 controller, Lincoln Electric R500 Power Wave welder, and a dual push pull wire feeder. The components are fully integrated to function as a seamless metal AM system. The manufacturing of a component is driven by its G-Code command file. G-Code describes the sequence of wire deposition for growing the component. The system adjusts to the substrate surface deformation by modifying the vertical location of the printing head. Between every interruption of wire deposition, the printing head is automatically cleaned. The work cell is equipped with a 2D positioner which also serves as a print table. It allows for printing objects with a footprint of up to 0.8x0.8 meters. Build plates are mounted on the print table and serve as the surface where the printed parts are built. The build plates are restrained to the table by toe clamps.

In mBAAM, the printing head, which is mounted on the end of the arm, moves to the starting point. The starting point is the beginning of the bead. The printing head then starts laying down material, which follows the geometric path created by the slicer while continuously depositing metal. When it reaches

the end of the bead, it stops and travels to the beginning of the next bead. Therefore, a bead is a path of continuous depositions. All beads deposited at the same vertical plane form a layer. The next layer beads are deposited on top of the previous layer/beads. The process continues until all the layers have been laid down.

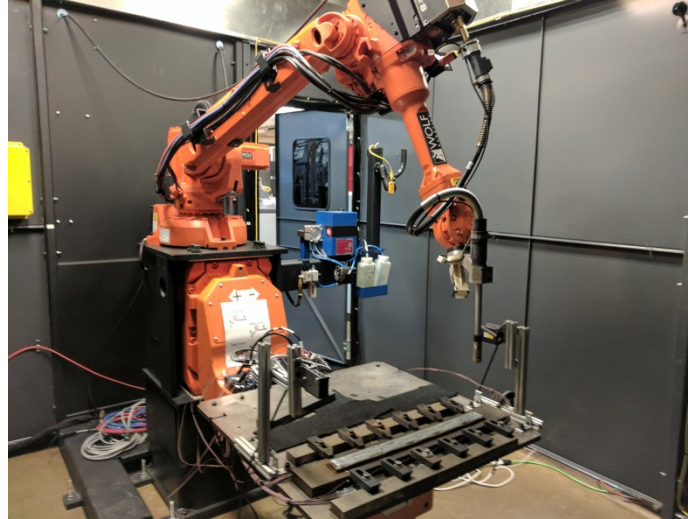


Figure 1: mBAAM equipment setup. The first manufactured object consists of four layers of deposited metal on a clamped build bar (center bottom of the image).

Three different experiments were conducted to support the development of the FEM simulation framework. The goal was to simulate predominantly one-dimensional (1D) and two-dimensional (2D) thermal and mechanical responses and to calibrate the model parameters before analyzing the manufacturing of complex three-dimensional (3D) objects. The 1D-like objects, named curl bars, were made by depositing four layers of material along the length of the build bar (Figure 1). Each layer consisted of a contour pass along the perimeter of the layer and a continuous fill-in of the layer. There was a total of eight traversals in the longitudinal direction (four continuous back and forth movements, with lateral offset). The 2D-like build object was a rectangular, thin wall build on a fully clamped build bar and was made of 124 layers. Each layer consisted of two parallel, continuous, and longitudinal beads that started at alternating ends to achieve consecutive layers. CAD models were created for all the printed objects, build plates, and the station table. They were exported as stereolithography (STL) files and then sliced using the slicer software. The slicer was customized to meet specifics of the mBAAM process. It divides the motion of the printing head into sequences of printing and travel motions. The resulting G-Code is translated into arm-welder specific commands.

In the first curl bar experiment, the build plate was mounted to the table using two non-symmetrically placed toe clamps (Figure 2a). The build plate was mounted this way to allow for unconstrained deformation of the plate in the long axis. Through this technique, distortions can be measured. In the second curl bar experiment, configuration of the plate was held uniformly by an array of clamps (Figure 2b). In the third experiment (Figure 2c), the plate was also held in place uniformly by a similar array of clamps.

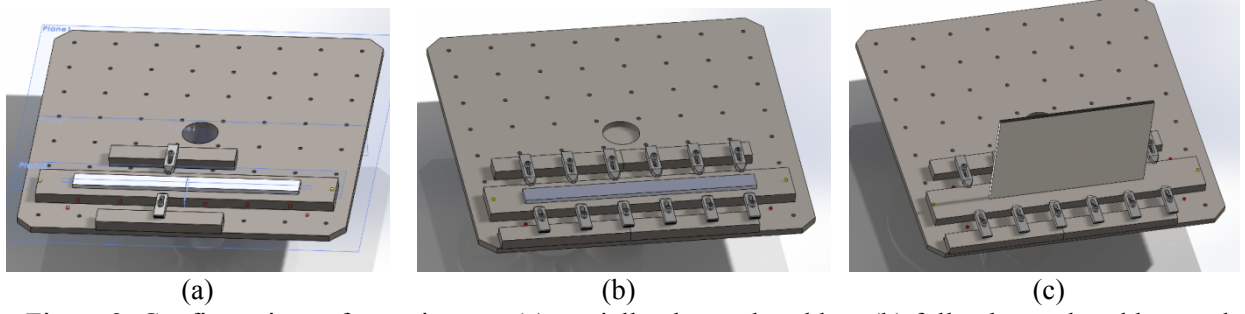


Figure 2: Configurations of experiments: (a) partially clamped curl bar, (b) fully clamped curl bar, and (c) thin wall bar

A total of 20 thermocouples were used in each test. Six thermocouples were drilled into each side of the build plate. Additionally, three thermocouples were attached to the table on each side of the build plate. One thermocouple was installed on the bottom of the table, and one was installed in the center, below the surface of the table. The thermocouple locations are depicted in Figure 3a. Two laser range finders were mounted above the ends of the build plate (Figure 3a, b) to measure their displacement.

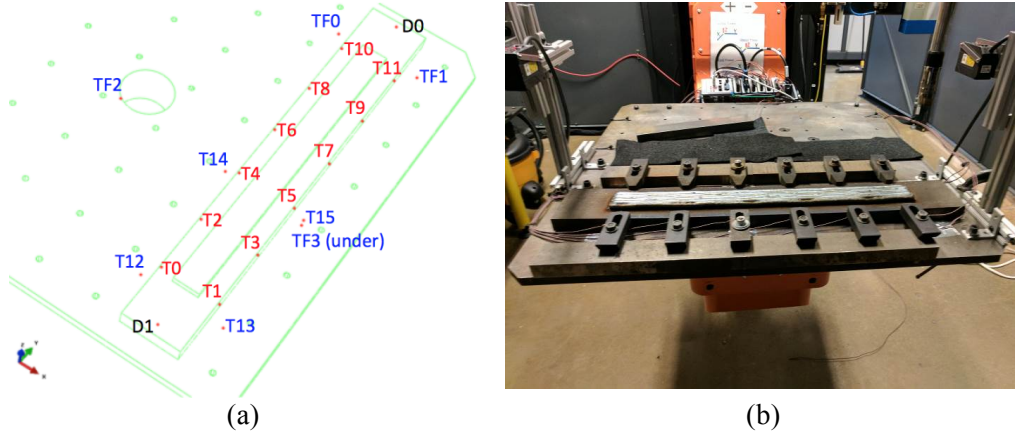


Figure 3: Experiment instrumentation: (a) locations of the thermocouples in the build bar (T0-T11), thermocouples on the print table (T12-TF3), and range finders (D0, D1), (b) test configuration.

A National Instruments C-RIO 9035 embedded system was used to collect and synchronize data. It was equipped with digital, analog, and thermocouple dedicated interfaces. The digital inputs were used to acquire the status of the printing head. The analog interfaces were used to read the displacement sensors and thermocouple inputs from the 20 thermocouples. A custom application was created to acquire, display, and save data. The data was collected at a frequency of 1Hz throughout the duration of the print. The print task time was variable and dependent on the part size and print conditions. Print times lasted from just over one hour (3600 samples points) to several hours. Single data samples consisted of 20 temperatures, two displacements, statuses of the deposition (on/off), and time stamps. The time stamping was necessary to synchronize the G-code information with the actual deposition sequence.

## 4. Methods

### 4.1 Physics-based Computational Framework

New physics-based FEM formulations and models implemented in Abaqus 2017 (from Dassault Systèmes) [16] were used in this study. It is not the focus of this paper to describe these features in detail, but key aspects of the framework include:

- A. Meshing: The geometric shape of the part whose 3D printing process is to be modeled is first discretized with finite elements. Arbitrary mesh densities can be used as generated by existing pre-processors. Using existing meshing technologies greatly improves and streamlines the analysis process. This is especially important because AM fabricated parts typically have very complex shapes that do not allow the use of uniform or layer-conforming meshes (difficult to generate).
- B. Machine information: The 3D printing machine related information (e.g., powder recoating sequence, laser scan path, material deposition of the printing head, arc weld power, etc.) is pre-processed with no loss of accuracy from actual data as used by the physical machines. As far as the modeling process is concerned, no loss of accuracy is encountered by simplifying the information that the printing machine would actually use.
- C. A new ABAQUS Intersection Module is used to sweep through the finite element mesh with the tool path and heat source configurations. The intersection can be based on either the original shape of the part or the current shape of the predicted deformed/distorted shape of the part during the analysis.
- D. Progressive element activation: At any given point during the simulation, any finite element could be completely filled with mater, partially filled with matter, or completely empty. The software precisely keeps track of this evolution, keeps track of the mass inventory and distribution to account for the addition of the material during the printing
- E. Progressive heating computations: at any point in time, heat bursts are computed by taking into account the actual path and power distribution of the heat source (the arc weld in this case). An arbitrary number of heating events (characterized as a sequence of heat fluxes at given locations) are computed for an accurate representation of the heating source in both time and space.
- F. Progressive cooling via convection and radiation: partial facet areas are computed to allow for a very precise assessment of cooling related heat fluxes regardless of the finite element discretization. Radiation and convection cooling can be modeled on a continuously evolving surface that reflects the current shape of the part at any given point during the print.
- G. Openness: a comprehensive set of new APIs are available to access information computed inside the code. While solutions for all major AM processes are provided, users can tailor physics modeling needs corresponding the particular process, machine environment, etc.

The usual heat transfer and stress divergence balance equations are leveraged and will not be reviewed here. Both a point-concentrated and a distributed volumetric heat flux model semi-ellipsoid model heat source model [17] were considered. In the local  $x$ - $y$ - $z$  frame of the arc weld, where  $x$ -axis aligns with the arc weld moving direction, the laser heat source is described as

$$Q(x, y, z, t) = \frac{2P\eta}{\bar{a}\bar{b}\bar{c}\pi\sqrt{\pi}} \exp \left[ - \left( \frac{(x + v_x t)^2}{\bar{a}^2} + \frac{(y)^2}{\bar{b}^2} + \frac{(z)^2}{\bar{c}^2} \right) \right] \quad (1)$$

Where  $P$  is the nominal power,  $\eta$  is the absorption coefficient, and  $v_x$  is the moving speed of the laser;  $t$  is the time;  $\bar{a}$ ,  $\bar{b}$ , and  $\bar{c}$  are the dimensions of the ellipsoid along  $x$ -,  $y$ -, and  $z$ -axes, respectively. The dimensions can be defined by laser parameters, including radius  $r$ , eccentricity  $e$ , and penetration depth  $d$ , as

$$\bar{a} = er, \quad \bar{b} = \frac{r}{e}, \quad \bar{c} = d \quad (2)$$

Thermal radiation:

$$q_{rad} = \epsilon\sigma((T - T_z)^4 - (T_\infty - T_z)^4) \quad (3)$$

and surface convection:

$$q_{conv} = h(T - T_\infty) \quad (4)$$

of free surfaces during manufacturing processes are considered, where  $\varepsilon$  is the material emissivity,  $h$  is convective coefficient,  $\sigma = 5.67 \times 10^{-8} \text{ W}/(\text{m}^2 \cdot ^\circ\text{C}^4)$  is the Stefan-Boltzmann constant,  $T_z = -273.15^\circ\text{C}$  is the absolute zero temperature, and  $T_\infty$  is the ambient temperature.

As for the material properties, temperature dependent material models for conductivity, specific heat, thermal expansion, and elasticity from the software's model library were chosen. For the purpose of this study a simple Mises plasticity model was also used for the mechanical response.

## 4.2 mBAAM Models

The models for the printed part include all the elements associated with the finished product. A model assembly of the printed part, build plate, and table plate was created based on the configuration as described in the experimental setup. Figure 4 shows this assembly for one of the curl bar models. In the model of the printed part and build plate share the same nodes at the connection, but in reality, they are welded to each other. At the interface where the build plate is partially clamped to the table, contact gap conductance  $0.5 \text{ mW}/\text{mm}^2/^\circ\text{C}$  for the contact region is assumed in the process simulation.

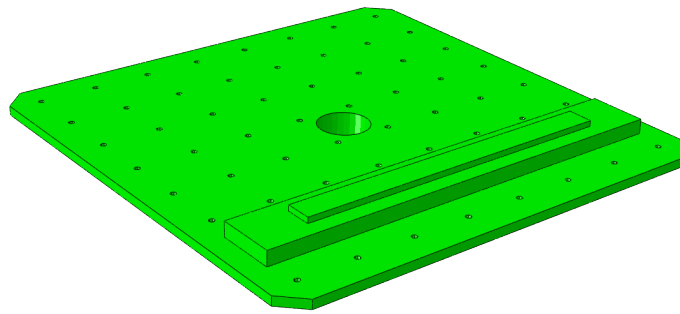


Figure 4: AM FEM model for the curl bar experiment

The positioner table is a large plate made from AISI 1020 steel. The build bars are made from AISI 1018 steel. The test objects are printed with mild steel and copper coated welding wire from Lincoln Electric, ER70S-6 [18]. The chemical composition of the three materials is very similar so that their thermal properties were assumed to be identical. One of the difficulties in weld modeling is the lack of measurements of thermal properties at high temperatures for even these simple materials. Thermal conductivity and heat capacity were derived based on carbon composition from reference [12], liquidus and solidus temperatures, latent heat from reference [19], and the coefficient of thermal expansion from reference [18]. The temperature-dependent mechanical properties for 1018 and 1020 steels were taken from reference [20].

Thermal conductivity as the function of temperature was used from Heinze et al. [19], reference Figure 3a for ferrite/bainite/martensite. Specific heat capacity was used from the same source [19], reference Figure 3b for ferrite/bainite/martensite. Liquidus and solidus temperatures, and latent heat were taken from reference [20]. The coefficient of thermal expansion was taken from Touloukian [21], reference Figure and Table No 275R. The temperature dependent mechanical properties for 1018 and 1020 steels were taken from Chen et al. [22], reference Table 5. The mechanical properties of the welding wire ER70S-6 were approximated by the properties of S355J2 steel [20], which has a similar chemical composition [23], reference Table 4. S355J2 steel has a similar chemical composition as ER70S-6 and is commonly welded by this wire.

The ambient temperature is taken as  $22^\circ\text{C}$ . The constant values of convection film coefficient  $0.018 \text{ mW}/\text{mm}^2/^\circ\text{C}$  is used for the printed part, and  $0.015$  or  $0.02 \text{ mW}/\text{mm}^2/^\circ\text{C}$  is used for the build plate. The heat source absorption coefficient is  $0.7$ . These values were approximated based on the range of

values used in the literature [9, 24]. The temperature and configuration dependence, although available in the software, were not taken into account. The objective of this study was to make a preliminary evaluation of the new simulation methods and formulations for mBAAM. Therefore, we tried to simplify the models associated with boundary conditions. Accordingly, the heat transfer coefficient between the build plate and the table was assumed constant and present in the region of the assumed thermal contact. This region is dependent on the build plate constraints and evolving deformation and was one of the calibration parameters in this study. The actual values are configuration and temperature dependent [9, 25]. As discussed, those were not taken into account. There were no Dirichlet boundary conditions applied in the heat transfer analysis because none of the pieces in the experiment were thermostated. Therefore, convection and radiation occurs on all surfaces.

The positioner table and the build plate involved in the experiments act as significant heat sinks, so they have to be modeled reasonably well. The overall dimensions of the positioner table are 812.8mm x 812.8mm x 15.875 mm and were modeled using hex elements. For the curl bar experiments, the build plate dimensions are 736.6mm x 101.6 x 25.4 mm and were modeled using hex elements. The printed part (558.8mm x 45mm x 10 mm) had to be modeled more carefully, and the size of the hex elements was chosen to correspond with the deposited layer height of 2.5 mm. The in-plane dimensions were taken such that the aspect ratio of the elements is reasonable. For the thin wall experiments, the build plate dimensions were 736.6mm x 101.6mm x 25.4 mm, and the printed part was 420mm x 9mm x 300 mm. Similar meshing considerations applied as above.

One of the key aspects of the new, physics-based framework in the software is that it does account with no loss of accuracy for the actual tool path information and energy information as used by the actual machine. The data from the analysis is derived directly from the G-code used by the physical machine in a neutral format that can be easily inspected. It accounts for all the pauses in the printing process associated with tool clean up and servicing. Two speed/power settings were used in most cases. For the first layer, the printing average speed was 4.2333 mm/sec, and the average power was 2720 Watts. For subsequent layers, the average speed was 6.7733 mm/sec, and the power was 2430 Watts.

### **4.3 Arc Weld AM Simulation**

In arc welding additive manufacturing, wire-fed consumable material is injected into a high focused energy source. The moving energy source is modeled with heat flux of prescribed nominal power. The high intensity heat source follows the experimentally recorded tool path, heats, melts, and fuses the consumable and substrate materials. As the material and the component go through the melting and solidification cycles, it accumulates residual stress and distortion, which are more critical in mBAAM than in conventional AM processes.

In the sequentially coupled heat transfer and stress analysis, the material melted by the arc weld as the wire steel is progressively added into the finite element simulation as the printing head follows the build path. The highly transient heat transfer balance is performed and temperature evolutions are calculated as the build progresses. These temperature distributions (time and space) are then used in a stress analysis static analysis to evaluate stresses and distortions. The effect of stress of the component on the temperatures is neglected.

## **5. Results**

Most of the analyses were performed on the curl bar models, and below we show results only from the more challenging partially clamped case depicted in Figure 2a. Only a quick preview of results obtained for the thin wall experiment (Figure 2c) are shown as its tool path data was only recently available. We conclude this section with brief review of the large part of interest, a printed excavator arm.

## 5.1 Partially Clamped Curl Bar

To compare the simulation with experimental results, we extracted the time histories of temperature at 12 locations (T0-T11 in Figure 3a) and the displacement history at locations D0 and D1. Figures 5-7 show the comparisons for the temperature histories at the 12 locations between the experimental results (all in red, labelled \*\_test) and simulation results for two convection coefficients,  $h=0.02$  and  $0.015$   $\text{mW}/\text{mm}^2/^\circ\text{C}$ . Even with these simple choices of constant convection coefficients, the curves compare reasonably well (although, there is certainly room for improvement). The cooling heat fluxes are computed on the evolving surfaces while accounting for the precise current exposed area.

At the left section of build plate at T0 and T1 in Figure 3(a) and (b), the simulation using  $h=0.015$  (in green) match well with the test data (in red); whereas at T2 and T3 in Figure 3(c) and (d), the simulation using  $h=0.02$  (in blue) (i.e. more convection and hence more cooling) match better with the test data.

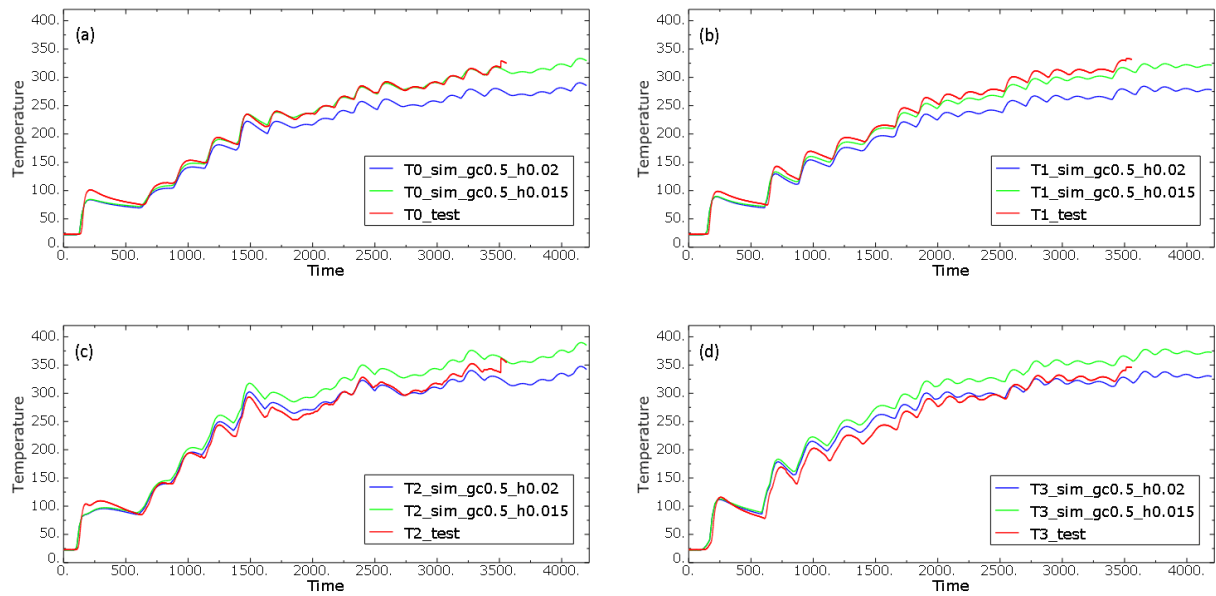


Figure 5: Temperature history comparison between the test and simulation results at thermocouple (a) T0, (b) T1, (c) T2, and (d) T3 on the build plate.

In the middle section of build plate, thermocouples T4 and T5 near the clamps and at T6 and T7 in Figure 6, the simulation using  $h=0.02$   $\text{mW}/\text{mm}^2/^\circ\text{C}$  matches data slightly better.



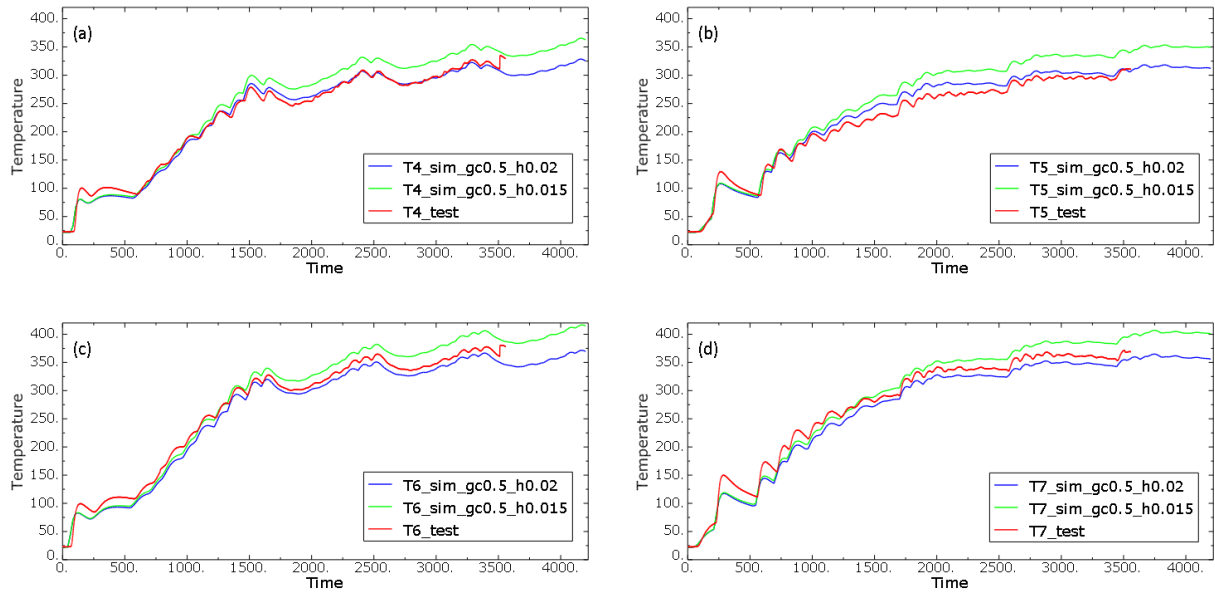


Figure 6: Temperature history comparison between the test and simulation results at thermocouple (a) T4, (b) T5, (c) T6, and (d) T7 on the build plate.

On the right section of the build plate, the T8-T11 thermocouples in Figure 7 are shown. The simulation using  $h=0.015 \text{ mW/mm}^2/\text{C}$  results in a slightly lower temperature than the test data. A better match can be obtained by decreasing the convection coefficient for less cooling in this section. This indicates the space-dependent convection coefficients may be needed for a better correlation. This choice may be motivated by the use of thermal blankets in the experiment to protect measurement equipment but more investigations are needed.

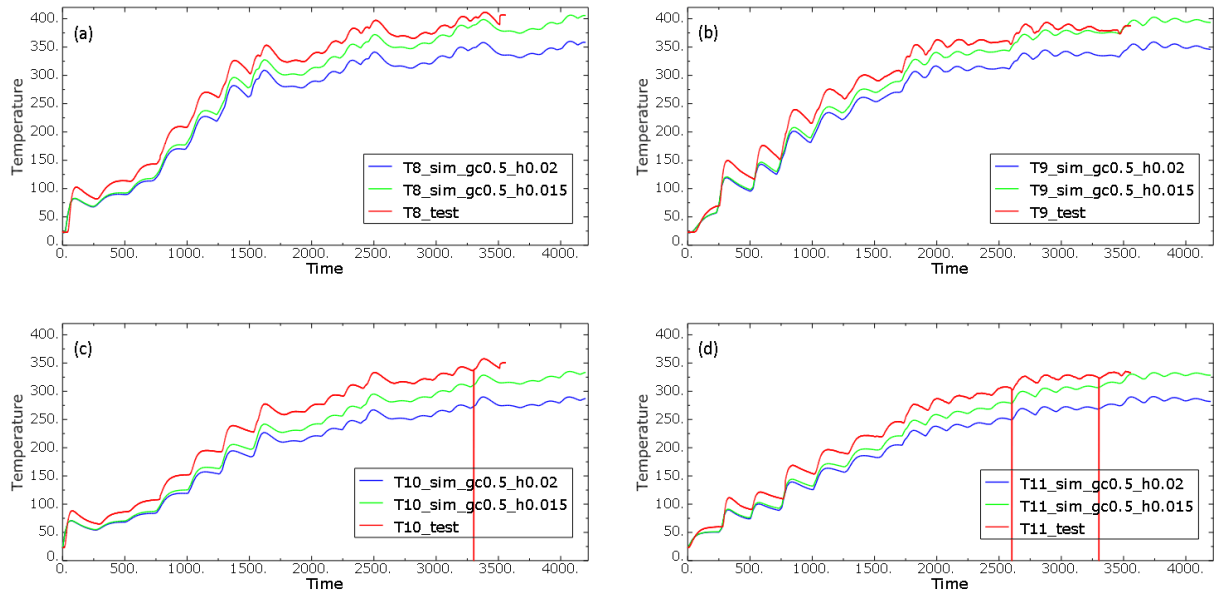


Figure 7: Temperature history comparison between the test and simulation results at thermocouple (a) T8, (b) T9, (c) T10, and (d) T11 on the build plate.

Despite the minimal calibration effort, the far range temperatures seem to correlate reasonably well with either choice of convection coefficients. A contour plot on the temperature field shortly after the printing has ended is shown in Figure 8a.

The previously obtained temperature histories were mapped (space and time) into a subsequent static analysis. The part experiences and overall upward bend/distortion as illustrated by the experimental curves in Figure 9. The molten material is added at the top of the printed part, and after a brief thermal expansion period (during each bead being deposited), the top experiences a contraction because of cooling to an ambient temperature, and this causes shortening. The final computed configuration of the build plate onto which the upward displacements are measured is shown in Figure 8b.

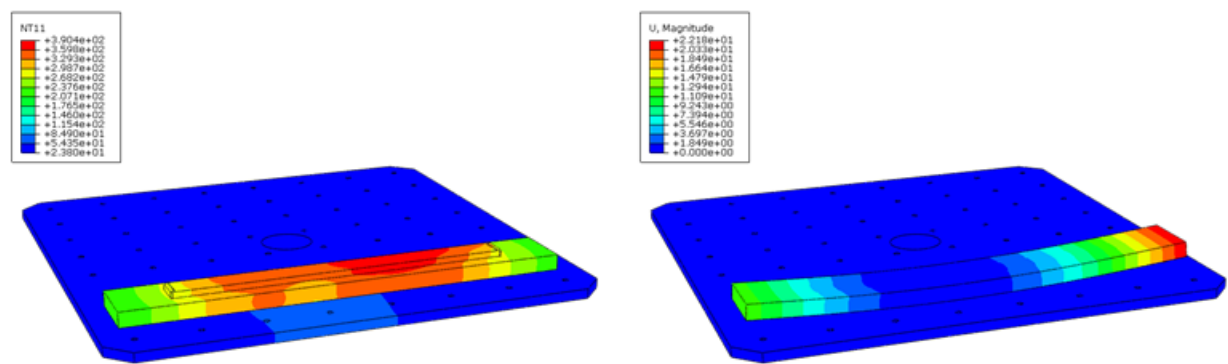


Figure 8: (a) Left: Temperature shortly after printing (in Celsius); (b) Right: Deformation after printing.

The evolving bending trend was shown by the time history of measured displacement at D0 and D1 on the build plate (Figure 9). The computed displacements at locations D0 and D1 are plotted against the experimental measurements. No attempt was made to calibrate any of the material parameters including the coefficients of thermal expansion. However, the deformation trends are captured correctly, although there is room for improvement. Upcoming work will improve on this correlation as well as compare overall scanned deformation profiles for the entire part.

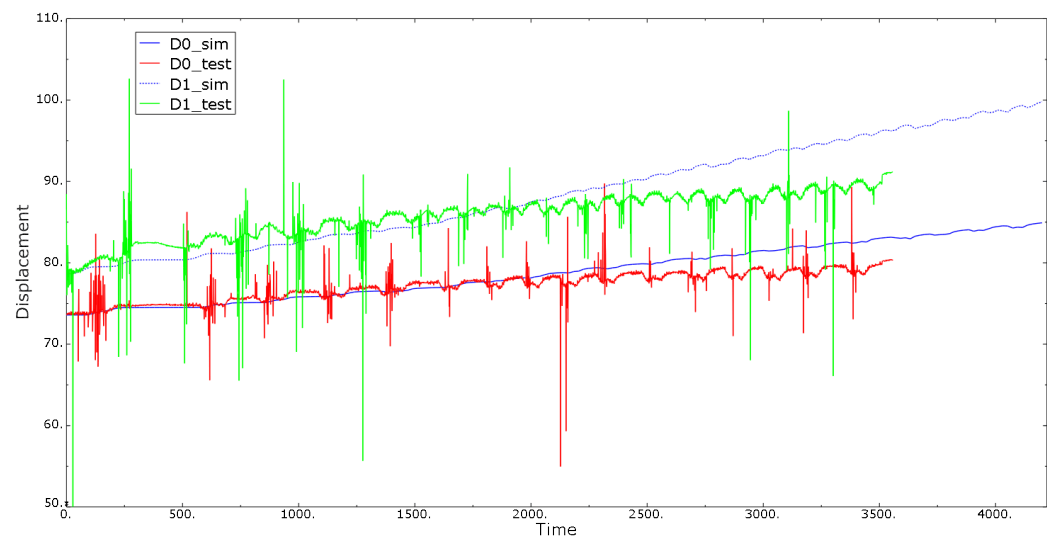


Figure 9: Displacement histories comparison between the test and simulation results at D0 and D1 on the build plate.

## 5.2 Thin Wall

Only preliminary results can be shared at this point as the experiment and simulations were conducted recently. Figure 10 shows temperature contour plots at various stages during the more than five hour print. A rather coarse time increment of 55 seconds for a total of 344 increments was used. As in any transient FEM analysis, the reported solution (in this case temperatures) reflect all sources for heating and cooling during the increment. In the early stages, there is more conduction into the massive build plate and positioning table. Therefore, the temperatures reflect a lower equilibrium temperature. As the print builds up and the overall temperatures increase, the intensity of the heat conduction from the heat source into the build plate and table is reduced, and the temperature contour plots reflect a higher equilibrium temperature.

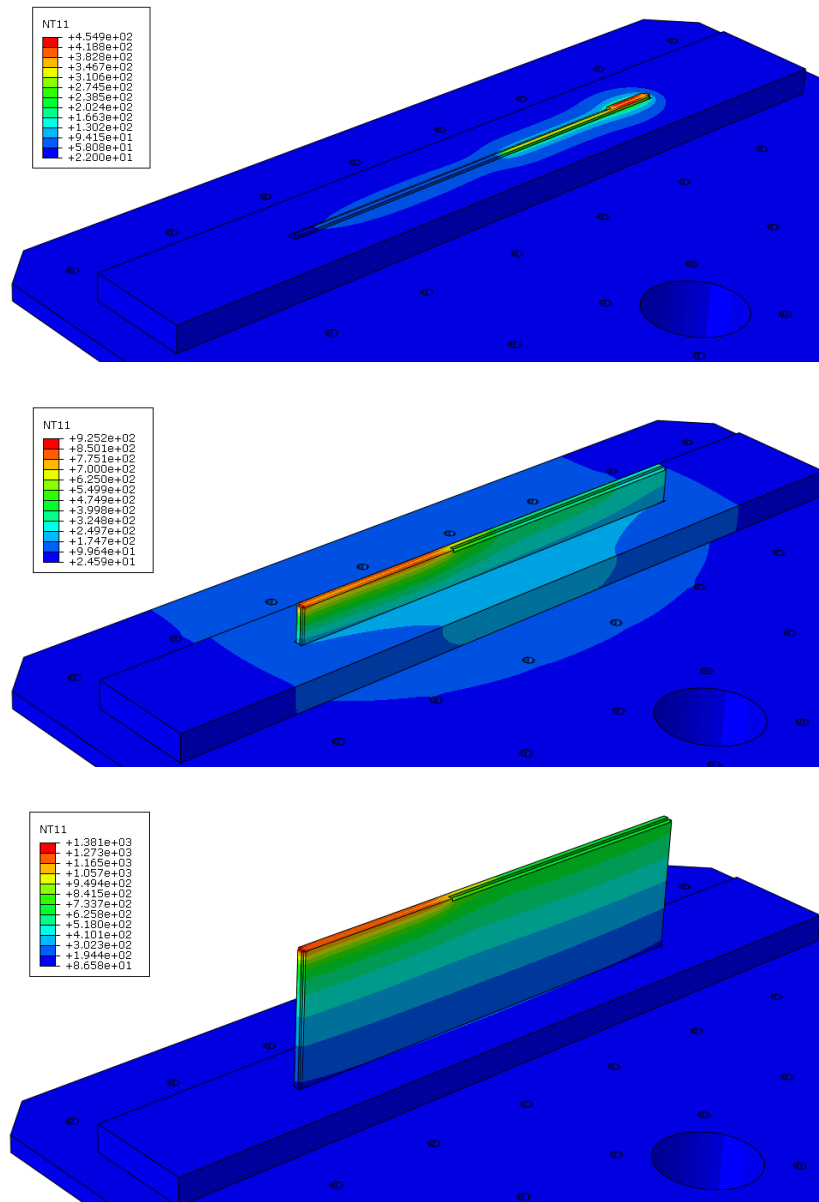


Figure 10. Thin wall thermal contour plots at various stages during printing

Using the same constant film coefficients as for the curl bar case,  $h=0.02$  and  $h=0.015$   $\text{mW/mm}^2/^{\circ}\text{C}$  for the printed part and the build bar, respectively, the simulated temperatures again match very well the experimental thermocouple data for the first hour of simulated printing. Afterwards, the simulations

exhibit faster cooling rates when compared to the experiment. Ongoing work includes developing better convection models (nonlinear temperature dependence) to capture more accurately the observed cooling rates.

### 5.3 Excavator Arm

The final goal of the ongoing computation analysis is to assess whether simulation tools can be used successfully in predicting temperature, distortion, and residual stress evolutions in very large parts. In Figure 11 depicts the part of interest. Figure 11a shows a photograph of the actual two-meter high part, and Figure 11b shows the corresponding FEM model.

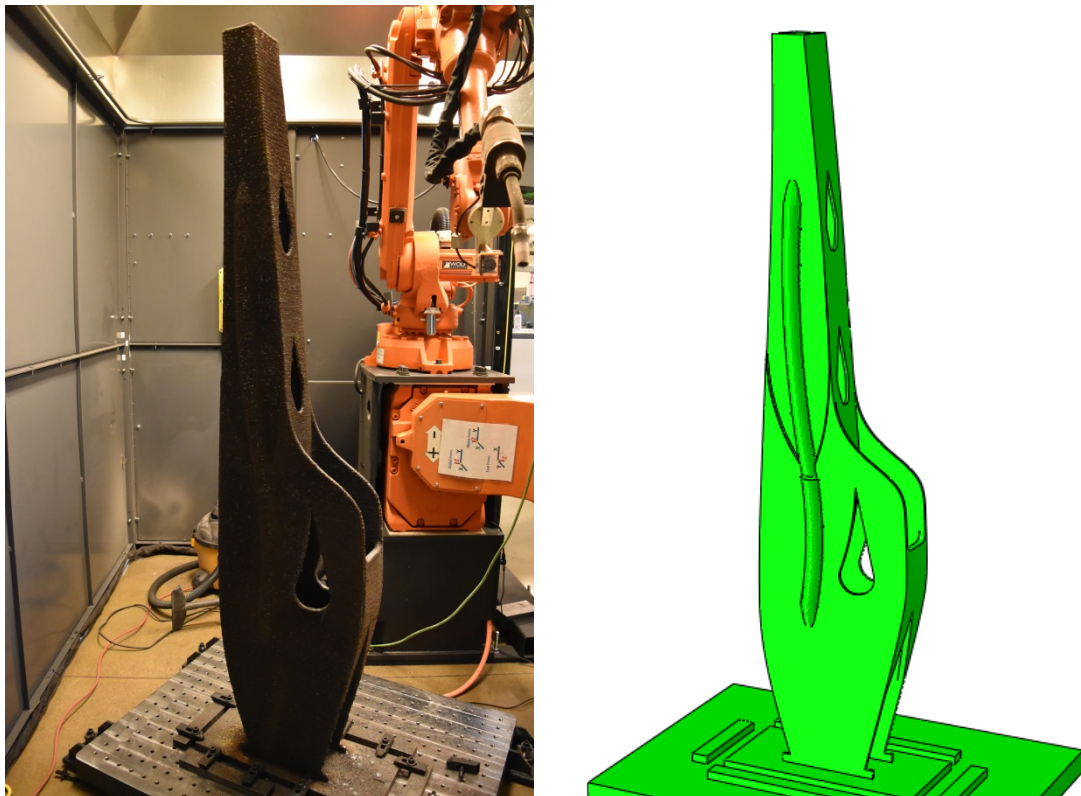
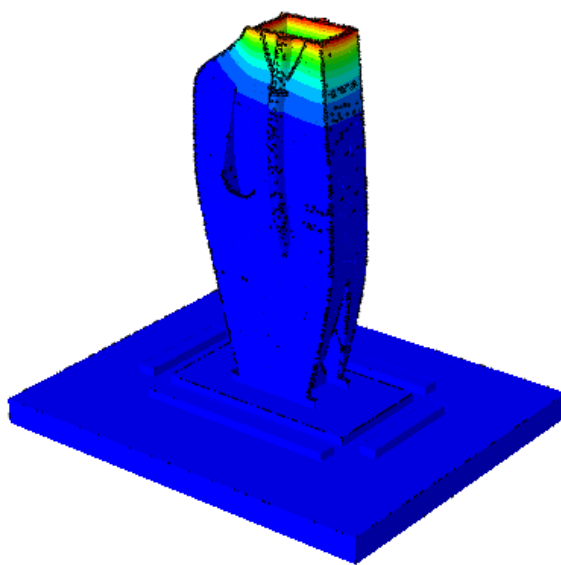
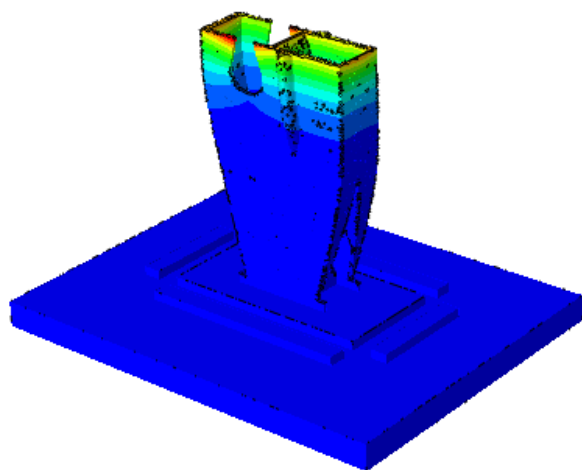
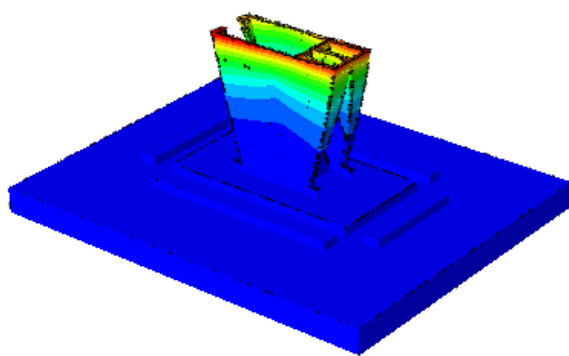
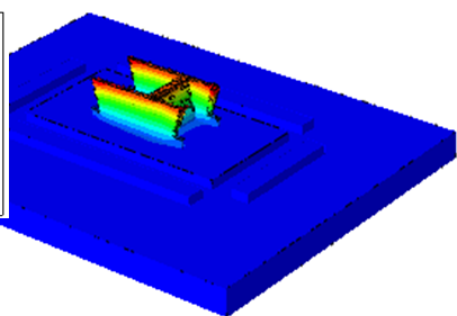
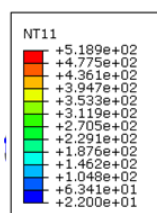


Figure 11: (a) Left: Photo of the printed excavator arm; (b) Numerical model.

The 70 hour print was a tremendous challenge and was very costly, so undertaking much experimentation is not possible. In Figure 12 we show preliminary results of the simulated temperature evolutions at various stages during the print. Aside from being able to assess the final distortions or residual stresses in the printed part, the goal is to computationally investigate various printing strategies. The overall goal is to minimize the distortions during printing allowing for the print to achieve acceptable final properties.



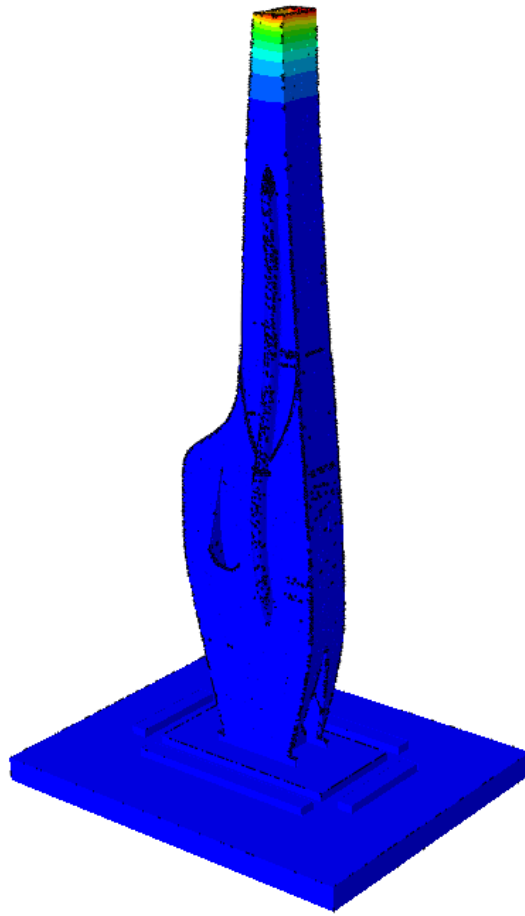


Figure 12: Preliminary results for temperature contour plots at several stages during print.

## 6. Conclusions

In this work we have presented initial efforts related to Metal Big Area Additive Manufacturing (mBAAM), a new AM technology exploring the feasibility of wire-feed continuous arc weld technology for large printed parts with high mass deposition rates in metal applications. Initial experimentation includes three sets of experiments from “small” (0.1 m high) to “large” (2m high). The “small” parts served dual purpose of gaining understanding of best practices on how best to operate the machine and to calibrate coefficients used for numerical modeling work. The simulation of large excavator arm demonstrates the feasibility of computational modeling for practical manufacturing problems using mBAAM.

Numerical modeling, as in many other applications, can be a cost-effective tool in gaining insight into the formidable multi-scale/multiphysics challenges that AM process in general, and mBAAM in particular, pose. We have presented initial work in numerical modeling of the mBAAM process leveraging a new physics-based framework implemented in a general-purpose FE code (Abaqus/Standard). Initial results show promise that numerical tools can be of assistance. With minimal calibration efforts a decent correlation with the simplest physical experiment (curl bar) was achieved. Preliminary numerical results for the other two applications were also shown.

Much remains to be explored. Ongoing work includes improving calibration for the heat transfer models and, directly related, distortion predictions for the curl bar experiment. With the improved heat transfer models, verification exercises will be performed against experimental test data for the thin wall experiment followed by the predictions of temperature histories and distortions for the excavator arm.

## 7. References

- [1] D. H. Ding, Z. X. Pan, D. Cuiuri, and H. J. Li, "Wire-feed additive manufacturing of metal components: technologies, developments and future interests," *International Journal of Advanced Manufacturing Technology*, vol. 81, pp. 465-481, Oct 2015.
- [2] D. H. Ding, C. Shen, Z. X. Pan, D. Cuiuri, H. J. Li, N. Larkin, *et al.*, "Towards an automated robotic arc-welding-based additive manufacturing system from CAD to finished part," *Computer-Aided Design*, vol. 73, pp. 66-75, Apr 2016.
- [3] P. M. Dickens, M. S. Pridham, R. C. Cobb, I. Gibson, and G. Dixon, "Rapid prototyping using 3-D welding," in *The Seventh Annual Solid Freeform Fabrication Symposium*, Austin, TX, 1992.
- [4] Y. A. Song, S. Park, D. Choi, and H. Jee, "3D welding and milling: Part I - a direct approach for freeform fabrication of metallic prototypes," *International Journal of Machine Tools & Manufacture*, vol. 45, pp. 1057-1062, Jul 2005.
- [5] S. Suryakumar, K. P. Karunakaran, A. Bernard, U. Chandrasekhar, N. Raghavender, and D. Sharma, "Weld bead modeling and process optimization in Hybrid Layered Manufacturing," *Computer-Aided Design*, vol. 43, pp. 331-344, Apr 2011.
- [6] J. Ding, P. Colegrove, J. Mehnen, S. Ganguly, P. M. S. Almeida, F. Wang, *et al.*, "Thermo-mechanical analysis of Wire and Arc Additive Layer Manufacturing process on large multi-layer parts," *Computational Materials Science*, vol. 50, pp. 3315-3322, Dec 2011.
- [7] J. A. Goldak and M. Akhlaghi, *Computational Welding Mechanics*: Springer, 2005.
- [8] N. Yadaiah and S. Bag, "Effect of Heat Source Parameters in Thermal and Mechanical Analysis of Linear GTA Welding Process," *ISIJ International*, vol. 52, pp. 2069-2075, 2012.
- [9] X. W. Bai, H. O. Zhang, and G. L. Wang, "Improving prediction accuracy of thermal analysis for weld-based additive manufacturing by calibrating input parameters using IR imaging," *International Journal of Advanced Manufacturing Technology*, vol. 69, pp. 1087-1095, Nov 2013.
- [10] A. S. Azar, S. K. As, and O. M. Akselsen, "Determination of welding heat source parameters from actual bead shape," *Computational Materials Science*, vol. 54, pp. 176-182, Mar 2012.
- [11] F. Cverna, *Thermal Properties of Metals*, ASM ready reference. Materials Park, OH: ASM International, 2002.
- [12] S. Yafei, T. Yongjun, S. Jing, and N. Dongjie, "Effect of Temperature and Composition on Thermal Properties of Carbon Steel," *Ccdc 2009: 21st Chinese Control and Decision Conference, Vols 1-6, Proceedings*, pp. 3756-3760, 2009.
- [13] M. Abid and M. Siddique, "Numerical simulation to study the effect of tack welds and root gap on welding deformations and residual stresses of a pipe-flange joint," *International Journal of Pressure Vessels and Piping*, vol. 82, pp. 860-871, Nov 2005.
- [14] J. Xiong, G. J. Zhang, H. M. Gao, and L. Wu, "Modeling of bead section profile and overlapping beads with experimental validation for robotic GMAW-based rapid manufacturing," *Robotics and Computer-Integrated Manufacturing*, vol. 29, pp. 417-423, Apr 2013.
- [15] D. H. Ding, Z. X. Pan, D. Cuiuri, and H. J. Li, "A multi-bead overlapping model for robotic wire and arc additive manufacturing (WAAM)," *Robotics and Computer-Integrated Manufacturing*, vol. 31, pp. 101-110, Feb 2015.
- [16] "ABAQUS Analysis User's Manual," Dassault Systemes Simulia Corp. 2017.
- [17] J. Goldak, A. Chakravarti, and M. Bibby, "A new finite-element model for welding heat-sources," *Metallurgical Transactions B-Process Metallurgy*, vol. 15, pp. 299-305, 1984.
- [18] T. L. E. Company, "Lincoln ER70S-6," T. L. E. Company, Ed., ed. Cleveland, OH, 2016, pp. 1-2.

- [19] C. Heinze, A. Pittner, M. Rethmeier, and S. S. Babu, "Dependency of martensite start temperature on prior austenite grain size and its influence on welding-induced residual stresses," *Computational Materials Science*, vol. 69, pp. 251-260, Mar 2013.
- [20] J. W. H. Price, A. Ziara-Paradowska, S. Joshi, T. Finlayson, C. Semetay, and H. Nied, "Comparison of experimental and theoretical residual stresses in welds: The issue of gauge volume," *International Journal of Mechanical Sciences*, vol. 50, pp. 513-521, Mar 2008.
- [21] Y. S. Touloukian, R. K. Kirby, R. E. Taylor, and P. D. Desai, *Thermal Expansion, Metallic Elements and Alloys* vol. 1975: IPI/Plenum, 1975.
- [22] J. Chen, B. Young, and B. Uy, "Behavior of high strength structural steel at elevated temperatures," *Journal of Structural Engineering-Asce*, vol. 132, pp. 1948-1954, Dec 2006.
- [23] J. Outinen and P. Makelainen, "Mechanical properties of structural steel at elevated temperatures and after cooling down," *Fire and Materials*, vol. 28, pp. 237-251, Mar-Aug 2004.
- [24] N. Pepe, S. Egerland, P. A. Colegrove, D. Yapp, A. Leonhartsberger, and A. Scotti, "Measuring the process efficiency of controlled gas metal arc welding processes," *Science and Technology of Welding and Joining*, vol. 16, pp. 412-417, Jul 2011.
- [25] M. P. Mughal, H. Fawad, and R. Mufti, "Finite element prediction of thermal stresses and deformations in layered manufacturing of metallic parts," *Acta Mechanica*, vol. 183, pp. 61-79, May 2006.